Journal of Building Engineering 49 (2022) 104068

Contents lists available at ScienceDirect

Journal of Building Engineering

journal homepage: www.elsevier.com/locate/jobe

Axial compressive performance of novel square coral concrete-filled duplex stainless steel tubes

Lan Rao [a,c], Qingrui Yue [a,b], Bin Huang [a], Xiaogang Liu [b,*]

[a] School of Civil Engineering, Xi'an University of Architecture & Technology, Xi'an, 710055, China
[b] Research Institute of Urbanization and Urban Safety, School of Civil and Resource Engineering, University of Science and Technology Beijing, Beijing, 100083, China
[c] Kaifeng University, Kaifeng, 475004, China

ARTICLE INFO

Keywords:
Axial performance
Composite column
Coral concrete
Stainless-steel tube

ABSTRACT

In this paper, a novel square coral concrete-filled duplex stainless steel tube (SCCFDSST) is proposed, and its axial compressive behavior is systematically investigated. Totally forty-five square steel columns welded with 2205 duplex stainless-steel plates are tested. Forty-two specimens are filled with coral concrete, and three columns are hollow steel tubes. The influential critical factors include the strength of coral concrete, the width-to-thickness ratio of steel tube and the constraint factor of SCCFDSST. The results indicate that SCCFDSSTs present satisfying ductility and bearing capacity. Moreover, the composite action provided by coral concrete and duplex stainless-steel tubes (DSST) is significant. For the purpose of guiding structural design, a mechanical model is established to determine the sectional capacity and the relationship between axial load and axial deformation of SCCFDSST. The accuracy of proposed formulas has been fully validated by experimental results, presenting higher precision than that of existing specifications. The results of this research can provide guidance for the application of the novel columns in engineering structures.

Nomenclature

A_s	Steel cross-sectional area
A_c	Concrete cross-sectional area
B	Width of square steel tube
DI	Ductility index
E_c	Concrete modulus of elasticity
E_s	Steel modulus of elasticity
f_{sy}	Yield strength of steel
$f_{c,28d}$	Concrete prism strength at 28 days
f_c	Concrete prism strength at specimen test day
N	Axial load
N_{max}	Ultimate load

* Corresponding author.
E-mail address: liuxiaogang@ustb.edu.cn (X. Liu).

https://doi.org/10.1016/j.jobe.2022.104068
Received 28 October 2021; Received in revised form 13 January 2022; Accepted 16 January 2022
Available online 19 January 2022

N_{uc}	Predicted ultimate strength
N_{ue}	Experimental ultimate strength
N_{b}	Local buckling load
DSS	Duplex stainless steel
SI	Strength index
t	Wall thickness of steel tube
σ	Stress
σ_{u}	Ultimate tensile stress
ε	Strain
ε_y	Strain corresponding to the strain $\sigma_{0.2}$
ε_{ue}	Experimental ultimate strain
μ_s	Poisson's ratio of steel
ξ	Confinement factor $\xi = A_{\mathrm{s}} \cdot f_{\mathrm{sy}} / (A_{\mathrm{c}} \cdot f_{\mathrm{c}})$
ρ	Steel content $\rho = A_{\mathrm{s}} / (A_{\mathrm{s}} + A_c)$

1. Introduction

Marine infrastructure construction is necessary for economic development, resource development, national sovereignty and security. However, the construction of marine structures is confronted with substantial challenges. First of all, natural environmental factors, including dry-wet circulation, seawater splashing and freeze-thaw phenomenon, severely deteriorate the durability and service life of traditional building materials [1,2]. Besides, long-distance transportation of traditional aggregate and freshwater also significantly increases the construction cost. Therefore, the demand for marine infrastructure construction using locally available materials with guaranteed quality has risen in recent years.

The coral reef is a special type of rock formed by accumulating calcareous remains and calcareous algae. It has been proved that this kind of reef can be used as the concrete aggregate [3–7]. In contrast, the concrete mixed with coral reefs, debris, coral sand, reefs, and seawater can be significantly cost-effective. Meanwhile, Minimize the construction period and pollution to the local environment [8]. Coral aggregate is similar to natural light aggregate but different from ordinary concrete and light aggregate concrete. In general, it belongs to lightweight, porous, and water-absorbing material with large surface areas [9,10]. At present, the basic mechanical properties of coral concrete have been studied [11,12]. However, the structural performance of coral concrete, which is more significant for engineering applications, needs to be investigated in depth.

For civil infrastructures subjected to marine environment, chlorine corrosion is the foremost factor affecting the durability and service life. Dou et al. [13] stated that the chloride diffusion coefficient of coral concrete decreased exponentially with the increment of exposure time, and it was higher in the actual marine concrete structures than under laboratory conditions by three orders of magnitude. Wattanachai et al. [14] pointed out that owing to the presence of chloride, the steel corrosion in coral concrete was more serious than that in ordinary concrete. Kakooei et al. [15] studied the air permeability and corrosion behavior of steel, and concluded that the corrosion rate of steel in coral concrete was at least twice that of ordinary concrete. Therefore, some effective measures are needed to ensure the durability of coral concrete structures in the marine environment, such as filling coral concrete into corrosion-resistant steel tube. For balancing the material cost and corrosion resistance, it is a good choice to select 2205 duplex stainless steel (DSS) as the material of steel tube, which is the second-generation nitrogen-containing DSS composed of 22% chromium, 3% molybdenum, and 7% nickel. In the solid solution of DSS, the ferrite phase (α) and austenitic phase (γ) contents are roughly the same. Previous research results show that the steel has excellent characteristics, including a high strength ($f_{\mathrm{sy}} \geq 450$), excellent ductility ($\delta \geq 25\%$) [16], and chloride corrosion resistance [17], and its material properties and application technologies are also promising [18].

In this study, a novel composite structure composed of seawater coral concrete and high-strength corrosion-resistant steel is proposed to facilitate the infrastructure construction in marine environment. In this study, 45 hollow section steel tubes welded with DSS plates were designed, among which 42 were filled with coral concrete. The influences of the steel tube size and concrete strength on the axial compression behavior of the tested specimens were studied experimentally. The coral concrete strength, width-to-thickness ratio of the steel tube and constraint factor (ξ) were treated as crucial parameters in test design. The limitation of existing codes in predicting the axial bearing capacity of coral concrete-infilling DSST was discussed. According to the experimental observations, a simplified model for calculating the sectional bearing capacity and ultimate strengths of short composite columns was proposed.

2. Design of experimental specimens

2.1. Test specimens

In this section, totally 45 square steel tubes were designed. Each steel tube was made of four pieces of rectangular DSS plates. The length (L) of the stub column was specified to be three times the width (B) of the section to avoid the influence of overall buckling and end conditions [19]. The mechanical properties were determined by the standard tensile test method [20]. Average value of measured material properties of DSS with different wall thicknesses are listed in Table 1. Herein, t refers to the wall thickness, and $\sigma_{0.01}$ is the

stress at 0.01% plastic strain. $\sigma_{0.2}$ stands for the stress at 0.2% plastic strain, which generally equals to the nominal yield strength of stainless steels. σ_u is the ultimate tensile stress, E_s is the Young's modulus, $\varepsilon_{0.2}$, ε_u, ε_f correspond to the strains at the yield strength, ultimate tensile stress and the plastic strain at fracture, respectively.

The coral from the South China Sea islands was fragmented into irregular particles. After sieving, coral aggregate with a particle size ranging from 4.75 mm to 26.5 mm was utilized as the coarse aggregate. Coral aggregate with a particle size less than 4.75 mm was used as the fine gravel aggregate. The prism compressive strength and elastic modulus (150 mm × 150 mm × 300 mm prisms) at 28 days for coral concrete were measured according to material test specification [21]. The mix proportions and observed material properties are summarized in Table 2. The measured bulk densities of coral concrete at different strength levels, namely, C30, C40, and C50, were 2043 kg/m^3, 2133 kg/m^3 and 2305 kg/m^3, respectively.

The main parameters in the tested SCCFDSSTs were as follows: (1) concrete strength, C30, C40, and C50; (2) the ratio of width to wall thickness (B/t):11.8–65.1; and (3) constraint factor (ξ), ranging from 0.58 to 4.61. The experiment in this paper was carried out in two batches. The test results of the first batch showed that there is no significant difference in compression behavior between the two specimens in the same group, especially in the group with high steel content. Therefore, during the second batch test, only one specimen was set in some test groups, and the test schedules was revised and more groups with different parameters was investigated. These comparative parameters are detailed in Table 3.

The details of SCCFDSSTs are also listed in Table 3, in which 'S' represents square section, 'B', 't' and 'L' denote outer diameter, wall thickness and length of square tube, respectively. And 'C0' represents the empty tube without filled concrete, ξ denotes the confinement factor, it can be seen that the ξ ranges from 0.58 to 4.61, f_c is the concrete prism compressive strength measured at the same time as loading test. The "S-140-4-C40 *" specimen shown abnormal failure, which could be attribute to weld defects, resulting in sudden and simultaneous cracking of welds on four sides during loading.

Double inclined-plane butt welds were used for the side welds of steel tubes, and single fillet welds were used for the end welds between the endplates and tubes, with E2209T welding rods for all the welds. Schematic diagram of designed steel tubes is presented in Fig. 1, and h_f was determined according to GB50017-2017 [23]. The bottom plate of steel tube was welded first, and the cover plate was welded after the curing of the concrete core. Coral concrete was poured from the top. Then, the vibration was performed at the out surface of steel tubes. After 28 days of curing, there was no noticeable shrinkage of the coral concrete at the tube top, owing to the incorporation of slag [24]. However, some aggregate particles floated up, resulting in part of the coral concrete protruding beyond the top of the tube, as illustrated in Fig. 2. The coral concrete above the top of the tube was removed, while the low-lying areas were leveled with cement mortar and sealed with a cover plate for each specimen before loading tests.

2.2. Test set-up

All the specimens were tested with the aid of YAW-20000 testing equipment. Fig. 3 shows the Experimental instrumentation of stub column specimens. Two strain gauges were arranged at mid-height of each side of the specimen, and two linear voltage-displacement transducers with a range of 100 mm were for recording the axial deformation. Preloading procedure was performed with 10%–15% of the estimated load (N_{max}) of the specimen. At the initial loading stage, the force-controlled loading method was adopted, with a speed of 180 kN/min, and the load is held for 2 min whenever the load increases by 10% N_{max}, as presented in Fig. 4a. When loading to 70% N_{max}, the displacement-controlled loading method was adopted, with a speed of 0.5 mm/min before the ultimate load and 1 mm/min after the ultimate load, as shown in Fig. 4b. The test was terminated while the reaction force drops to 70% of N_{max} or the weld cracks appear.

In this paper, the data measured by the longitudinal strain gauge was mainly used to analyze the behavior of the specimen before loading to the bearing capacity, while the behavior after the bearing capacity was mainly analyzed by the results measured by the linear voltage-displacement transducers. The data measured by lateral strain gauges was used to qualitatively analyze the local buckling of steel tube and the restraint effect between steel tube and core coral concrete.

3. Analysis of experimental observations

3.1. Failure modes

The main failure modes of the DSST specimens filled with coral concrete were local buckling, weld fracture, and coral concrete crushing. In addition, double-wave buckling also occurred in a few specimens, as shown in Fig. 5. The test phenomena recorded during the test showed that most of the local buckling of SCCFDSSTs occurred after the peak load (N_{max}) in the decay stage, while a few SCCFDSSTs with higher steel content buckled before reaching peak load. For instance, specimens "S-140-12-C40", "S-160-12-C40", and "S-180-12-C40" locally buckled when loaded to 97%, 98%, and 99% of N_{max} before the peak load, while specimens "S-120-6-C30", "S-140-6-C30", and "S-160-6-C30" locally buckled when the load dropped to around 100%, 93%, and 86% of N_{max} in the decay stage,

Table 1
Mechanical properties of DSS2205.

t (mm)	$\sigma_{0.01}$ (MPa)	$\sigma_{0.2}$ (MPa)	σ_u (MPa)	E_s (MPa)	$\varepsilon_{0.2}$ (%)	ε_u (%)	ε_f (%)
3.84	356	581	747	200000	0.493	17.8	27.5
5.92	309	535	724	199420	0.470	27.8	41.8
7.80	311	542	736	198640	0.475	21.0	31.2
11.90	327	535	732	196040	0.474	22.2	33.5

Table 2
Mixture proportions and material properties of coral concrete.

Concrete	Mix proportions(kg/m^3)						$f_{c,28d}$	E_c	ε_c
	Cement	Slag	Silica	Coarse	Fine	Water	(MPa)	(MPa)	(με)
C30	280	90	30	800	800	287	35.7	23400	2000
C40	520	97.5	32.5	675	675	194	44.6	28500	2385
C50	640	120	40	625	625	212	53.8	31000	2600

Table 3
Comparative parameters for tested specimens.

No.	Specimen	L	B/t	ξ	f_c	N_{ue} (kN)		SI	DI
	label	(mm)			(MPa)	Measured	Average		
1	S-120-4-C30	360	31.3	1.88	43.8	1568	1578	0.99	2.49
2	S-120-4-C30	360	31.3	1.88	43.8	1598		1.01	1.95
3	S-140-4-C30	420	36.5	1.78	38.9	1732	1728	0.91	2.06
4	S-140-4-C30	420	36.5	1.78	38.9	1723		0.91	1.82
5	S-160-4-C30	480	41.7	1.37	43.8	2195	2177	0.91	1.58
6	S-160-4-C30	480	41.7	1.37	43.8	2158		0.90	2.12
7	S-200-4-C30	600	52.1	1.06	44.7	2981	2981	0.88	1.97
8	S-120-6-C30	360	20.3	2.82	43.8	2079	2079	1.06	7.33
9	S-140-6-C30	420	23.6	2.66	38.9	2151	2252	0.92	5.00
10	S-140-6-C30	420	23.6	2.66	38.9	2352		1.01	3.83
11	S-160-6-C30	480	27.0	1.99	44.7	2809	2809	0.96	2.72
12	S-120-8-C30	360	15.4	3.98	43.8	2823	2717	1.19	9.08
13	S-120-8-C30	360	15.4	3.98	43.8	2611		1.10	7.05
14	S-140-8-C30	420	17.9	3.30	43.8	3153	3107	1.08	5.39
15	S-140-8-C30	420	17.9	3.30	43.8	3061		1.05	4.95
16	S-160-8-C30	480	20.5	2.82	43.8	3864	3818	1.11	9.34
17	S-160-8-C30	480	20.5	2.82	43.8	3772		1.08	9.19
18	S-140-4-C40	420	36.5	1.33	52.4	2174	2050	1.02	1.15
19	S-140-4-C40*	420	36.5	1.33	52.4	1926		0.90	3.61
20	S-160-4-C40	480	41.7	1.15	52.4	2759	2603	1.06	1.16
21	S-160-4-C40	480	41.7	1.15	52.4	2446		0.94	1.41
22	S-180-4-C40	540	46.9	1.01	52.4	2872	2787	0.92	1.28
23	S-180-4-C40	540	46.9	1.01	52.4	2701		0.86	1.28
24	S-140-6-C40	420	23.6	1.89	54.8	2622	2666	1.01	5.37
25	S-140-6-C40	420	23.6	1.89	54.8	2709		1.04	1.92
26	S-140-8-C40	420	17.9	2.76	52.4	3338	3339	1.10	4.25
27	S-140-8-C40	420	17.9	2.76	52.4	3339		1.10	5.70
28	S-160-8-C40	480	20.5	2.25	54.8	3560	3636	0.96	5.32
29	S-160-8-C40	480	20.5	2.25	54.8	3711		1.00	4.98
30	S-180-8-C40	540	23.1	2.06	52.4	4296	4300	0.99	5.41
31	S-180-8-C40	540	23.1	2.06	52.4	4304		0.99	4.25
32	S-140-12-C40	420	11.8	4.61	52.4	5323	5323	1.34	12.52
33	S-160-12-C40	480	13.4	3.88	52.4	5667	5667	1.19	10.75
34	S-180-12-C40	540	15.1	3.35	52.4	6544	6544	1.18	8.29
35	S-140-4-C50	420	36.5	1.07	64.9	1987	1887	0.84	2.07
36	S-140-4-C50	420	36.5	1.07	64.9	1787		0.76	1.94
37	S-200-4-C50	600	52.1	0.73	64.9	3120	3120	0.75	1.72
38	S-250-4-C50	750	65.1	0.58	64.9	4484	4484	0.75	1.01
39	S-140-6-C50	420	23.3	1.59	64.9	2669	2669	0.97	5.63
40	S-160-6-C50	480	26.7	1.37	64.9	3181	3181	0.94	2.10
41	S-140-8-C50	420	17.5	2.22	64.9	3337	3344	1.04	7.08
42	S-140-8-C50	420	17.5	2.22	64.9	3351		1.03	4.44
43	S-140-4-C0	420	35.0	–	–	844	844	–	4.45
44	S-140-6-C0	420	23.3	–	–	1816	1816	–	3.80
45	S-140-8-C0	420	17.5	–	–	2683	2683	–	4.26

respectively. This is different from the behavior of concrete-filled mild-strength steel tubular composite columns, which may be attributed to the fact that DSS steel has no yield platform and its yield strain ε_y is about 4.7×10^3με, which is much higher than the peak compressive strain ε_c of coral concrete. When loaded to a certain load (corresponding to the curshing compressive strain of coral concrete), the concrete crushing leads to the decrease of its bearing capacity, while the bearing capacity of steel tube still increases with increase of its strain. When the width-thickness ratio is higher than a specific value (such as $B/t > 20$ in this paper), the increase of steel tube bearing capacity is not enough to supply for the loss of concrete's bearing capacity, and therefore the bearing capacity of composite column begins to decline, resulting in local buckling of steel tube due to the expansive action of crushed coral concrete infilled. Yet, when the width-thickness ratio is relatively smaller, the increase of steel tube bearing capacity will exceed the loss of

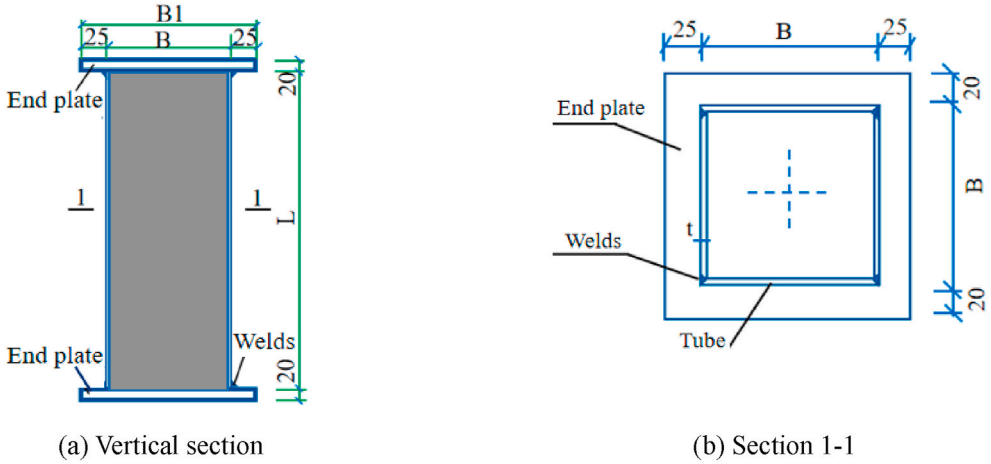

Fig. 1. Schematic diagram of steel tube.

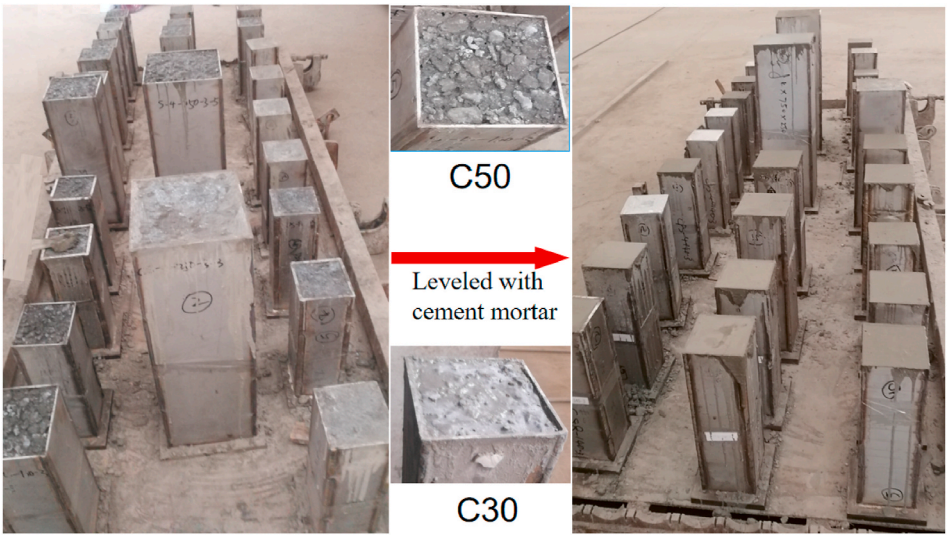

Fig. 2. Coral aggregate floating and leveled with cement mortar.

concrete's bearing capacity, resulting in the continuous growth trend of composite column bearing capacity. Also, the smaller width-thickness ratio of steel tube leads to a better constraint for the expansive action of crushed coral concrete infilled, and the steel tube exhibits later local buckling after its strain exceeds yield strain.

The location of local buckling is about 1/6-1/2 of the specimen height, which is not significantly with respect to the difference of the wall thickness t or section width B of the specimen. With the continuous growth of deformation, the core coral concrete at the buckling of steel tube expands outward and is crushed into powder, as shown in Fig. 5(d), which is obviously different from the crush mode of ordinary concrete. The crack of steel tube weld mainly occurs at the local buckling location, where the concrete is also seriously damaged.

3.2. Curves of load versus axial deformation

Figs. 6–8 show the relationship between axial load (N) and axial deformation (Δ) of the tested specimens. The ultimate loads (N_{max}) corresponding to each specimen are summarized in Table 3. It can be observed from Fig. 6 that the curves of specimens with small constraint factor (ξ) or large B/t ratio tend to exhibit a rapid downward trend after the ultimate load. Meanwhile, the specimens with greater ξ or smaller B/t ratios exhibit milder bearing decline. In addition, specimens with $\xi > 2.8$ or $B/t \leq 15$ exhibit obvious strengthing trend.

Further, Fig. 6 shows that the initial slope of the curves increases, the descending section becomes steeper, and the descending extent of ductility increases with the increase of outer diameter (B) of the steel tubes. It can be clearly seen from Fig. 7 that the ultimate load (N_{max}) and ductility of the SCCFDSSTs increase with the steel tube wall thickness (t). Moreover, the composite specimens with

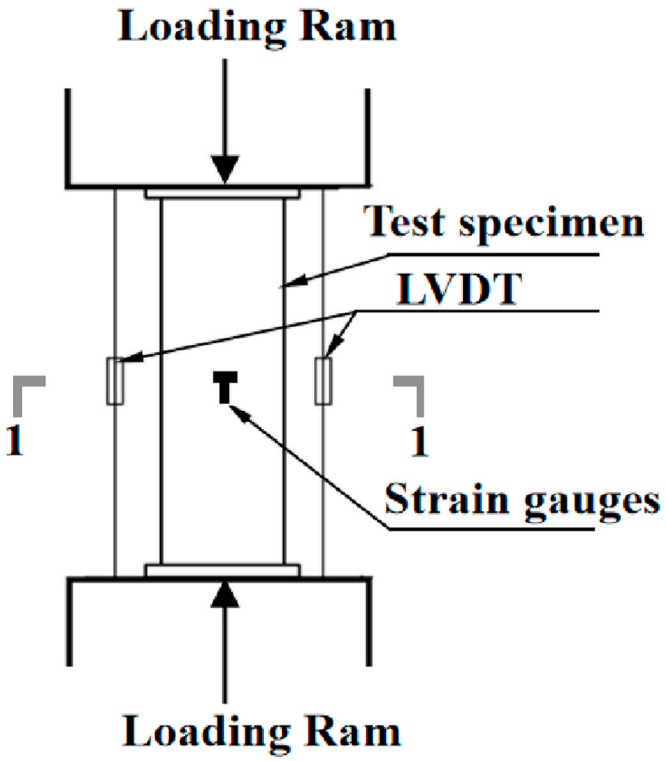

Fig. 3. Experimental instrumentation of stub column tests.

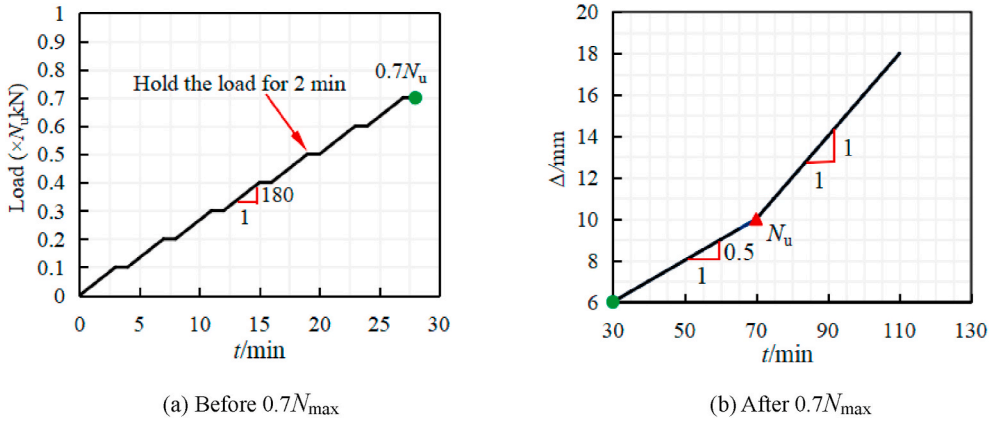

(a) Before $0.7N_{max}$ (b) After $0.7N_{max}$

Fig. 4. Loading system of stub column tests.

larger steel ratio present higher confinement effect, consistent with that of square CFST stub columns reported by Han et al. [19].

Compared to concrete strength, the influence of size variation of the steel tube on the performance of specimens is more evident, as shown in Fig. 8. When f_c is less than 50 MPa, the initial axial stiffness and ultimate load of the specimens increase slightly with the coral concrete strength. However, for cases in which f_c is greater than 50 MPa, the ultimate load of the specimens filled with C50 concrete is not apparently higher than that with C40 concrete. This would be attributed to the low strength and high brittleness of coral aggregate. When the stress of core concrete exceeded the strength of coral aggregate particles, the aggregate particles were crushed firstly, and the high porosity of coral aggregate delayed the transverse deformation of concrete, resulting in the reduction of the constraint effect of steel tube on core coral concrete.

3.3. Curves of load versus strain

Fig. 9 shows the relationship between reaction force and strain value at the middle section (Section 1-1 in Fig. 3) of the specimens with different widths or thicknesses. Most specimens show local buckling near the middle section, while a few specimens show local

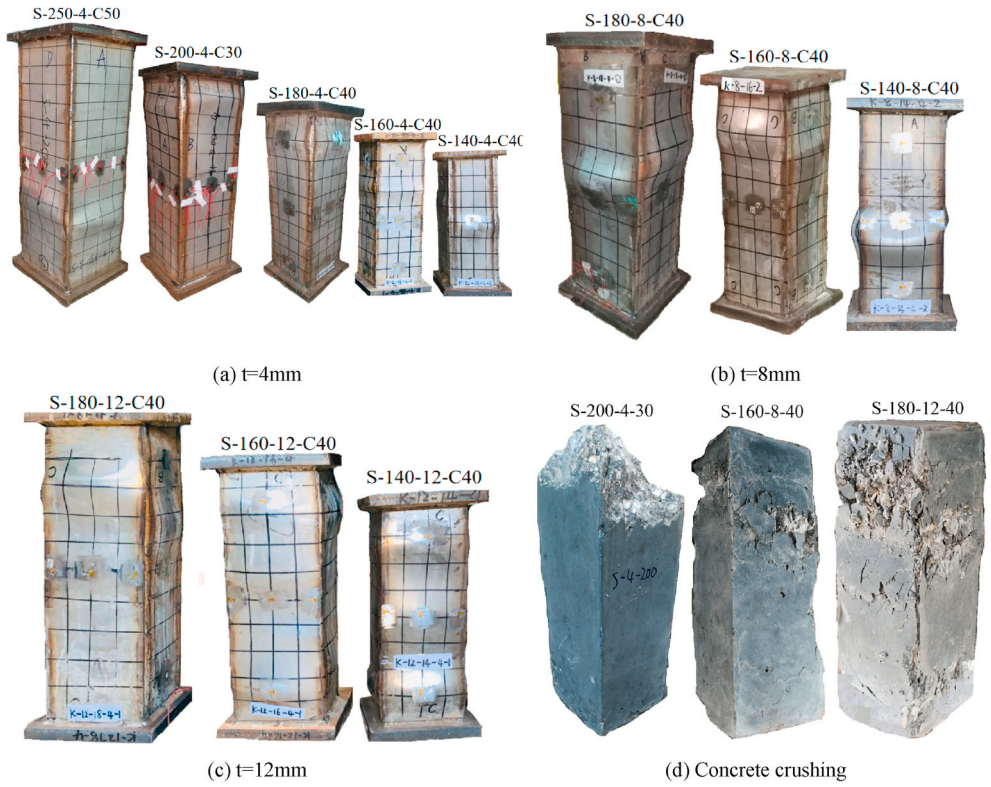

Fig. 5. Typical failure modes of specimens.

buckling close to end plates. It can be observed from Fig. 9 that specimens with high B/t ratios, such as "S-4-160-C40" and "S-4-140-C40", the steel strain at peak point is smaller than the yielding strain ε_y. However, for specimens with smaller B/t ratios, such as "S-8-160-C40" and "S-8-140-C40", the steel strain at peak point exceeds ε_y, indicating that the steel tube yielded before the peak load, which is consistent with the phenomenon observed during the test in Section 3.1. It should be explained that the measured longitudinal or transverse strain of some specimens was too small to reach its yield strain, as shown in Fig. 9a and b, which is mainly due to the fact that the buckling of the steel tube did not occur at the measuring point.

3.4. Lateral deformation coefficient (ν_{sc})

Fig. 10 summarizes the relationship between load ratio (N/N_{ue}) and lateral deformation coefficient (ν_{sc}) at the mid-height of composite specimens. It can be seen from Fig. 10 that before the load reaches 80% of N_{max}, the ν_{sc} of the composite specimens varies from 0.2 to 0.3, which is similar to that of the hollow steel tube columns. Further, when the load reaches 80%–90% of N_{max}, the lateral deformation coefficient of the specimens began to increase gradually and exceeded 0.5, indicating that the steel tube had a significant constraint effect on coral concrete. The calculated ν_{sc} of some specimen did not exceed 0.5, but it not indicated the constraint effect was poor. This is mainly due to the fact that the steel tube buckling did not occur at the measuring point.

3.5. Strength index

For quantitatively comparing the sectional strength, the strength index (SI) can be defined as follows:

$$SI = \frac{N_{ue}}{N_{u1}} \tag{1}$$

where: $N_{u1} = A_s f_{sy} + A_c f_{c,}$ as the sectional capacity calculation formula in EC4-2004 [25].

The intensity index (SI) calculated according to test measurement is listed in Table 3. Figs. 11 and 12 are the relationships of SI with ξ and B/t, respectively. It can be concluded from Figs. 11 and 12 that the strength index increases approximately linearly with the increase of ξ, and decreases with the increment of B/t, which are similar to that reported in collected literatures [26,27].

In addition, Figs. 11 and 12 indicate that the SI of SCCFDSSTs filled with C40 concrete is slightly higher than that with C30 concrete. However, the SI of SCCFDSSTs filled with C50 concrete is lower than that filled with C40 concrete, or even lower than that filled with C30 concrete, indicating that the material strength of coral concrete has limited effect on strength index of SCCFDSSTs.

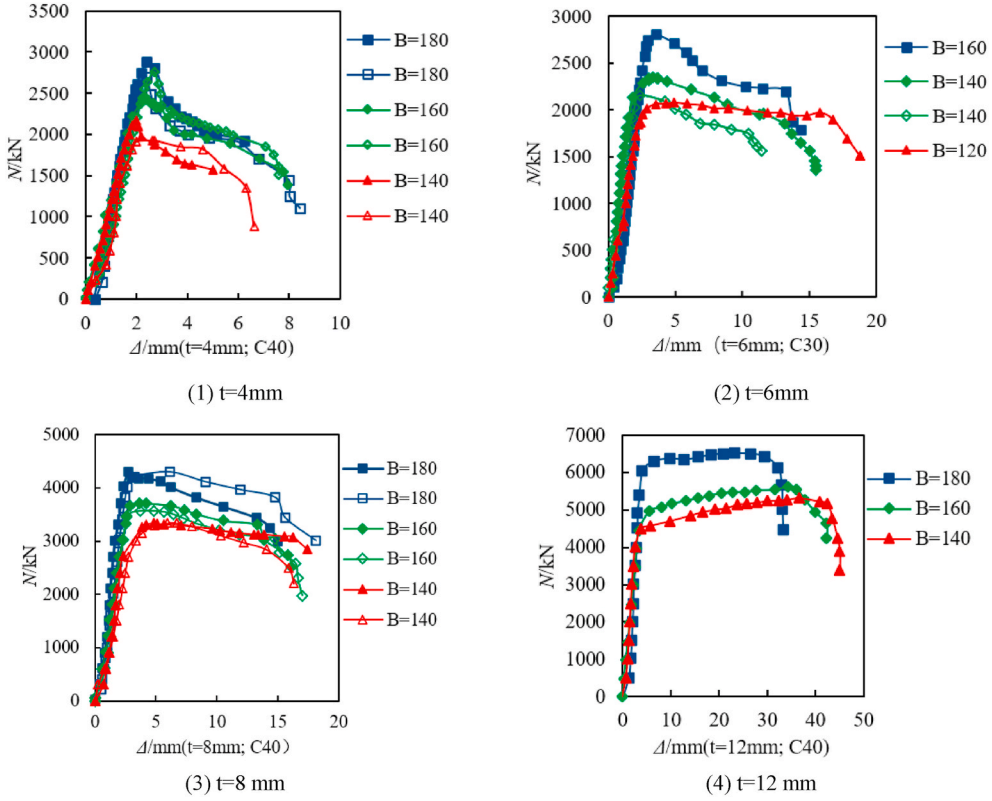

Fig. 6. Axial load (N) versus axial deformation (Δ) with different outer diameters.

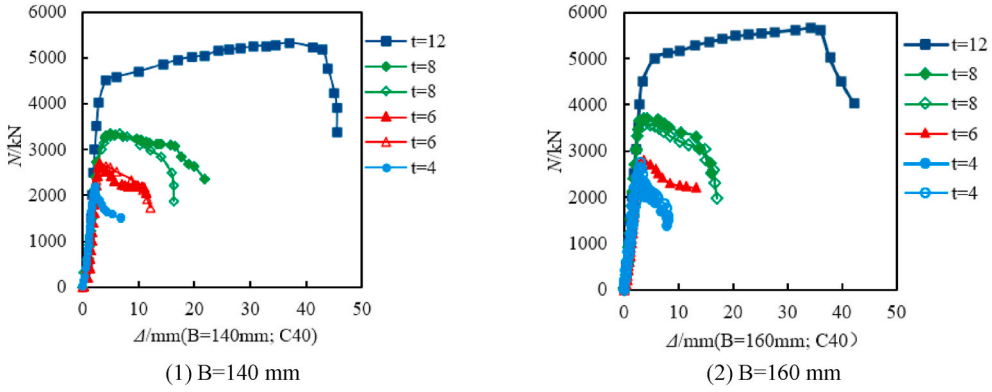

Fig. 7. Axial load (N) versus axial deformation (Δ) with different wall thickness.

3.6. Ductility index

The ductility index (*DI*) is one of the critical parameters for evaluating deformation performance of structures. In general, the load versus axial strain and load versus axial deformation curves are adopted for demonstrating ductility index [27,28]. In this study, the curves of load versus axial deformation were used to determine the ductility index [28], which is expressed as follows:

$$DI = \frac{\Delta_{85\%}}{\Delta_y} \tag{2}$$

$$\Delta_y = \frac{\Delta_{75\%}}{0.75} \tag{3}$$

where $\Delta_{85\%}$ is the axial deformation of the specimen when the load drops to 85% of N_{max}, and $\Delta_{75\%}$is the axial deformation of the

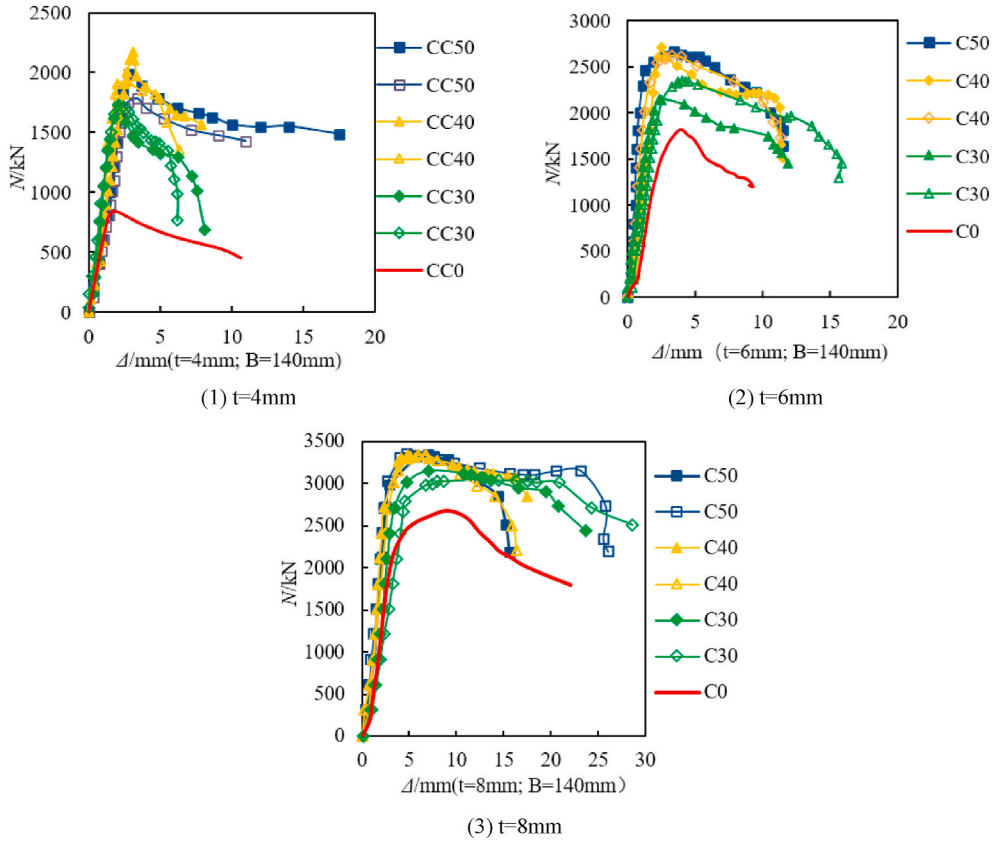

Fig. 8. Axial load (N) versus axial deformation (Δ) with different concrete strength.

specimen when the load rises to 75% of N_{max}.

The ductility index values are tabulated in Table 3, and DI versus ξ and DI versus B/t are plotted in Figs. 13 and 14, respectively. It can be observed that the ductility index increases approximately linearly with increase of ξ, but decreases nonlinearly with increase of B/t. As shown in Fig. 14, for $B/t < 30$, the ductility index decreases rapidly with the increase of B/t. For $B/t > 30$, the ductility index decreases slowly and gradually tends to be stable. However, the effect of coral concrete strength on DI is not significant.

3.7. Constraint factor

Fig. 15 shows the relationship between cross-sectional stress σ_{sc} (N/A_{sc}) and strain ε_L ($\Delta L/L$) of tested specimens with different constraint factors ξ in the middle span (Section 1-1 in Fig. 3). The critical constraint factor (ξ_0) is used to describe the minimum constraint requirement of CFST, which can guarantee the force gradually moves from concrete core to the steel tube during concrete crushing. As can be seen from Fig. 15, this factor for SCCFDSST is approximately 2.8. For $\xi > 2.8$, the curve of N/A_{sc}-ε of SCCFDSSTs shows greater strengthening with increasing ξ. If ξ close to 2.8, the N/A_{sc}-ε curve of SCCFDSST tends to be flat. For $\xi < 2.8$, the N/A_{sc}-ε curve shows greater decline with decreasing ξ. As ξ decreases, the bearing capacity decline becomes steeper, and appears earlier at smaller strain.

While the relationship between coral concrete cubic compressive strength and prism compressive strength is not quite certain [12, 22,30], the prism compressive strength f_c is used to calculate parameter ξ, as shown in the nomenclature table. Equivalently, the critical ξ_0 of SCCFDSST is approximate to that of traditional CFST, which is about 4.5 due to the fact that characteristic concrete strength f_{ck} is used for calculating parameter ξ and f_{ck} is defined as 0.67 f_{cuk} [29]. However, the equivalent critical constraint factor ξ_0 of SCCFDSST is still a bit smaller than that of traditional CFST, and this is mainly due to the fact that the internal friction angle of coral aggregate is much large than that of traditional aggregate, meaning that the crushed coral concrete can bears higher load than crushed traditional concrete with same constraint stress.

4. Mechanical model

4.1. Section capacity

Fig. 16 shows the relationship between axial stress ($\sigma_{sc} = N/A_{sc}$) and axial strain (ε) of SCCFDSSTs under different working conditions. For $\xi \geq \xi_0$, the σ_{sc}-ε curves exhibit the characteristics of strain hardening (Type I) or perfect elastic-plastic (Type II). For $\xi < \xi_0$, the σ_{sc}-ε curves show degenerate types (Type III). As per the method proposed by Han et al. [19], the load value corresponding to ε_{scy}

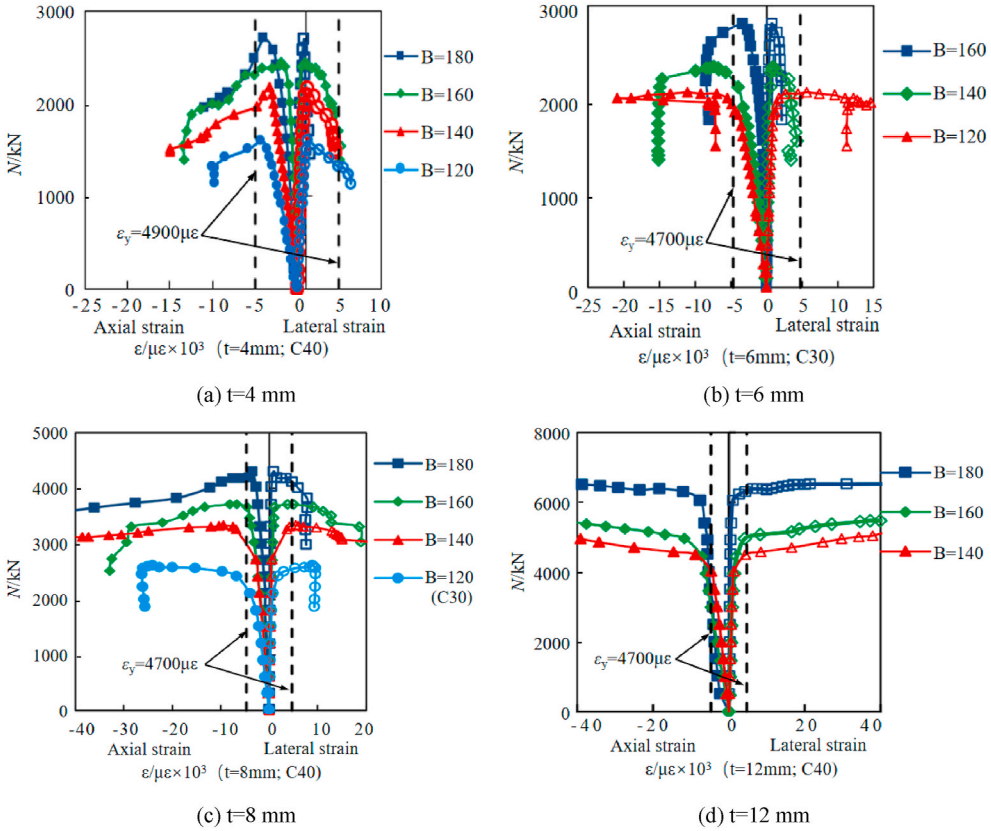

Fig. 9. Typical load versus strain curves in the middle section.

was selected as the bearing capacity of SCCFDSST in this study. According to these three different types of load-deformation relationships shown in Fig. 16, the value of ε_{scy} is determined by regression analysis method, as detailed in Eqs. (4) and (5).

For $\xi < 2.8$:

$$\varepsilon_{scy} = (900 + 24.5f_c) + (1000 - 0.5f_c)\xi^{3/2} - 200\xi^2 \tag{4}$$

For $\xi \geq 2.8$:

$$\varepsilon_{scy} = \varepsilon_{sy} \tag{5}$$

The determination of ε_{scy} (point B in Fig. 16) is mainly considered as follows:

(1) For the σ_{sc}-ε curves are of deterioration types (Type III), ε_{scy} is the strain corresponding to the peak load.
(2) While the σ_{sc}-ε curves show a perfect elastic-plastic behavior (Type II): a) For $\varepsilon \leq \varepsilon_{scy}$, the axial stress σ_{sc} increase rapidly with the increment of axial strain. b) For $\varepsilon > \varepsilon_{scy}$, the axial stress σ_{sc} increases or decreases slightly with the increase of axial strain, and then begin to present a flat development trend.
(3) For the σ_{sc}-ε curves exhibit strain hardening behaviors (Type I), the elastic-plastic stage of σ_{sc}-ε curve is basically complete at ε_{scy}, and then the stress increases linearly with strain, presenting strain hardening behavior. While the slope (E_{sch}) of the strain hardening section of the curve increases with the enlargement of ξ, it is much lower than the initial slope (E_{sc}).

For simplicity, the nominal yield strength (f_{scy}) of SCCFDSSTs is defined as follows:

$$f_{scy} = N_{ue}/A_{sc} \tag{6}$$

where N_{ue} is the sectional capacity of the composite column. A_{sc} is the cross-section area of composite section.

According to the test results in this paper, the compressive strength ratio of the composite section (f_{scy}/f_c) is linearly related to the constraint factor (ξ), as shown in Fig. 17. The formula of f_{scy} can be obtained by regression analysis method:

$$f_{scy} = (0.78\xi + 0.865)f_c \tag{7}$$

$$\xi = A_s f_{sy}/(A_c f_c) \tag{8}$$

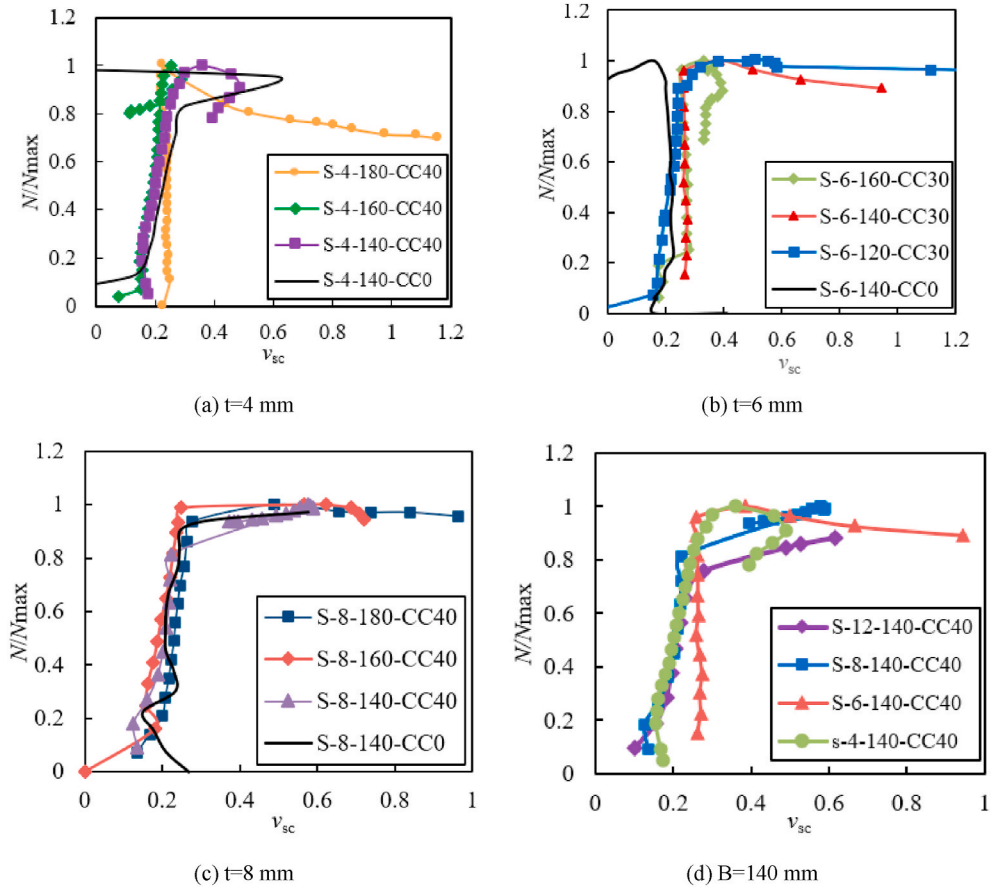

Fig. 10. Load ratio (N/N_{max}) versus lateral deformation coefficient (ν_{sc}).

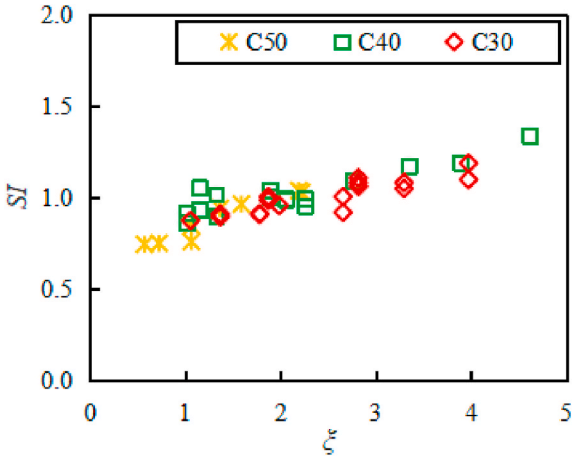

Fig. 11. ξ versus *SI*.

The validity limit of Eq. (7) is that the value of ξ ranges from 0.58 to 4.61. It can be found that Eq. (4) and Eq. (7) are significantly different from the analytical model proposed by Han et al. [19], due to the fact that the mechanical properties of coral concrete aggregate in the coral composite columns in this study are significantly different from those of traditional concrete aggregate.

Table 4 and Fig. 19 show that the results predicted with Eq. (8) are in good agreement with the test results, with a mean value of 1.004 and a COV (coefficient of variation) of 0.073. Therefore, the proposed method can be used to evaluate the bearing capacity of coral concrete-filled steel tube stub columns under axial compression.

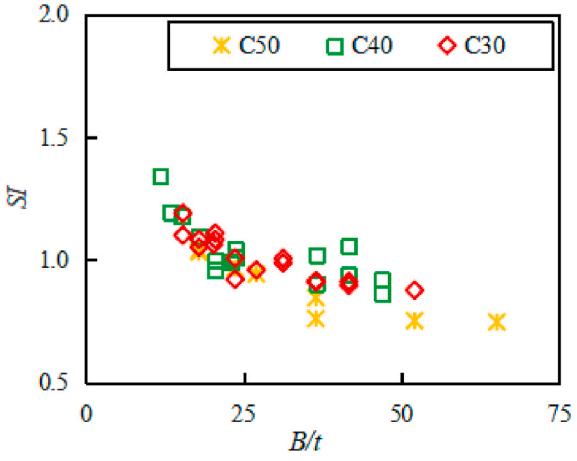

Fig. 12. B/t versus *SI*.

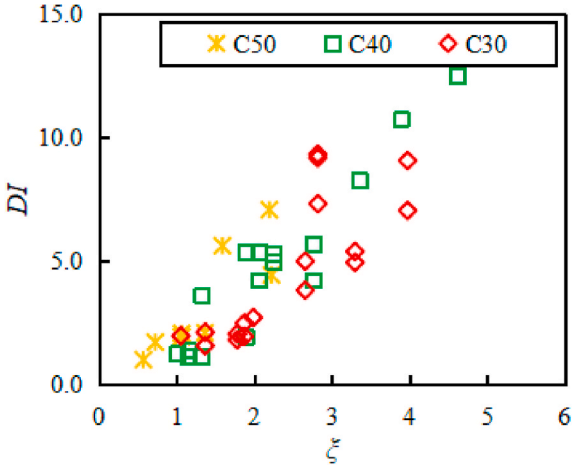

Fig. 13. ξ versus *DI*.

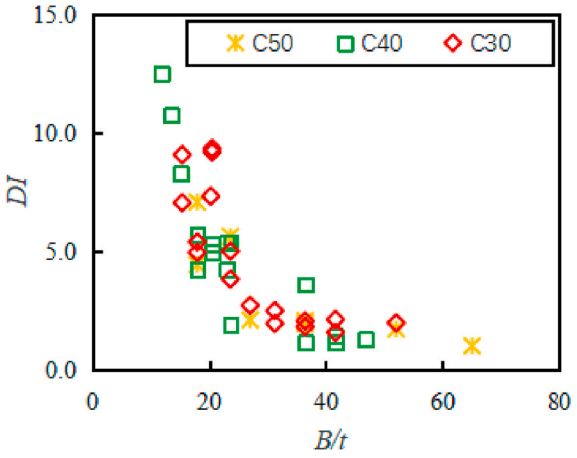

Fig. 14. *B/t* versus *DI*.

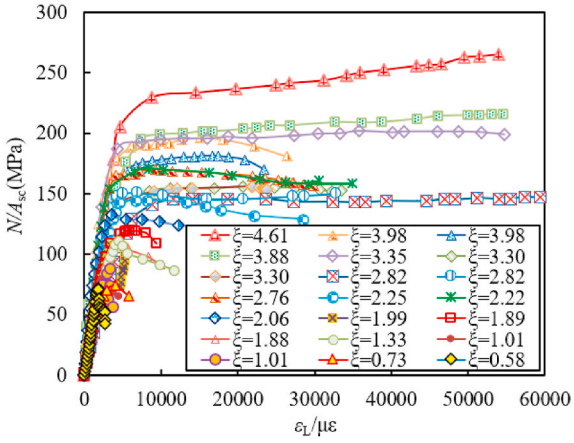

Fig. 15. Relationship of N/A_{sc} and ε_L.

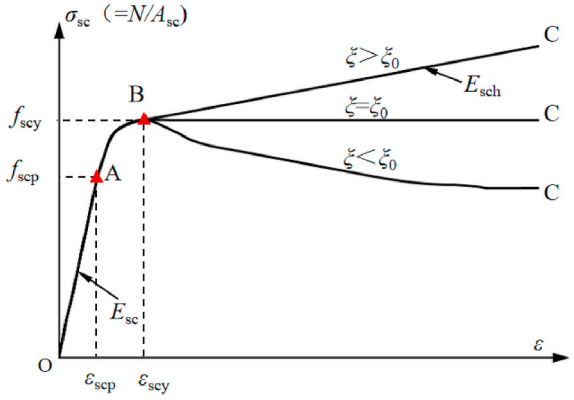

Fig. 16. Typical axial load (σ_{sc}) versus axial strain (ε).

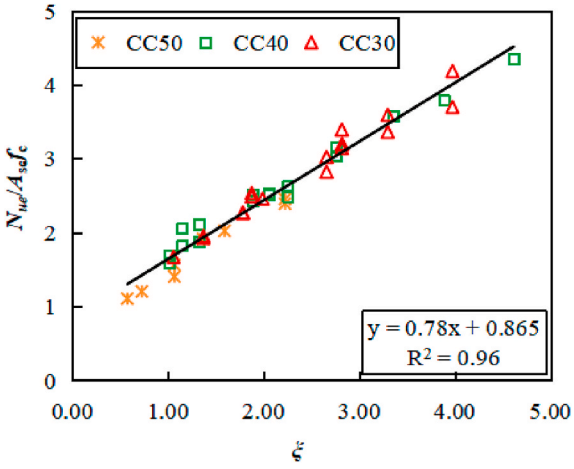

Fig. 17. $N_{ue}/(A_{sc}f_c)$ versus constraint factors (ξ).

4.2. Relationship between axial load and axial deformation

Based on regression analysis on the axial compression test results of 42 coral concrete filled square steel tube columns, the σ_{sc}–ε curves shown in Fig. 16 can be expressed as follows:

Table 4
Comparisons of predicted column strength and test results.

No	Specimen	N_{ue} (KN)	GB50936 N_{c1}/N_{ue}	DBJ13-51 N_{c2}/N_{ue}	EC4 N_{c3}/N_{ue}	AIJ N_{c4}/N_{ue}	BS5400 N_{c5}/N_{ue}	LRFD N_{c6}/N_{ue}	Proposed formulas N_{cp}/N_{ue}
1	S-4-120-C30	1598	1.077	1.095	0.994	0.878	0.663	0.801	0.919
2	S-4-120-C30	1568	1.097	1.116	1.013	0.894	0.676	0.816	0.936
3	S-140-4-C30	1723	1.208	1.193	1.100	0.971	0.729	0.885	0.998
4	S-140-4-C30	1732	1.201	1.187	1.095	0.966	0.725	0.880	0.993
5	S-160-4-C30	2187	1.234	1.202	1.102	0.968	0.701	0.877	0.992
6	S-160-4-C30	2158	1.251	1.218	1.116	0.981	0.711	0.889	1.005
7	S-200-4-C30	2979	1.305	1.248	1.142	1.000	0.698	0.900	1.015
8	S-120-6-C30	2017	0.963	1.119	0.971	0.895	0.681	0.793	0.959
9	S-140-6-C30	2151	1.116	1.219	1.087	1.000	0.757	0.886	1.042
10	S-140-6-C30	2305	1.042	1.138	1.014	0.934	0.707	0.827	0.972
11	S-160-6-C30	2809	1.111	1.169	1.044	0.955	0.702	0.843	0.984
12	S-120-8-C30	2638	0.783	1.090	0.900	0.837	0.654	0.742	0.948
13	S-120-8-C30	2331	0.886	1.233	1.019	0.948	0.740	0.840	1.073
14	S-140-8-C30	3083	0.893	1.109	0.945	0.876	0.674	0.775	0.957
15	S-140-8-C30	2883	0.955	1.186	1.010	0.937	0.721	0.829	1.023
16	S-160-8-C30	3523	0.984	1.138	0.990	0.915	0.694	0.808	0.975
17	S-160-8-C30	3802	0.911	1.054	0.917	0.848	0.643	0.749	0.903
18	S-140-4-C40	2175	1.096	1.088	0.980	0.861	0.621	0.779	0.896
19	S-140-4-C40*	1926	1.236	1.227	1.105	0.971	0.700	0.879	1.010
20	S-160-4-C40	2760	1.072	1.047	0.945	0.829	0.585	0.747	0.855
21	S-160-4-C40	2446	1.209	1.181	1.066	0.935	0.660	0.843	0.964
22	S-180-4-C40	2702	1.325	1.281	1.157	1.013	0.702	0.910	1.038
23	S-180-4-C40	2872	1.246	1.205	1.089	0.953	0.660	0.856	0.977
24	S-140-6-C40	2613	1.048	1.144	0.994	0.908	0.664	0.801	0.961
25	S-140-6-C40	2709	1.011	1.104	0.959	0.876	0.640	0.773	0.927
26	S-140-8-C40	3117	0.936	1.161	0.977	0.903	0.684	0.797	0.993
27	S-140-8-C40	3246	0.899	1.115	0.938	0.867	0.657	0.766	0.954
28	S-160-8-C40	3495	1.076	1.242	1.064	0.978	0.726	0.862	1.053
29	S-160-8-C40	3689	1.019	1.177	1.008	0.927	0.688	0.817	0.997
30	S-180-8-C40	4265	1.056	1.165	1.015	0.931	0.685	0.820	0.983
31	S-180-8-C40	4304	1.047	1.154	1.005	0.923	0.679	0.813	0.974
32	S-140-12-C40	4471	0.591	1.171	0.888	0.833	0.653	0.734	1.025
33	S-160-12-C40	5081	0.740	1.182	0.934	0.873	0.676	0.769	1.027
34	S-180-12-C40	6080	0.800	1.124	0.914	0.853	0.653	0.750	0.971
35	S-140-4-C50	1987	1.346	1.338	1.184	1.037	0.724	0.933	1.088
36	S-140-4-C50	1785	1.498	1.489	1.318	1.154	0.806	1.039	1.211
37	S-200-4-C50	3120	1.555	1.498	1.331	1.159	0.763	1.033	1.193
38	S-250-4-C50	4484	1.582	1.511	1.340	1.164	0.738	1.031	1.189
39	S-140-6-C50	2573	1.151	1.253	1.075	0.978	0.700	0.860	1.042
40	S-160-6-C50	3181	1.167	1.225	1.062	0.962	0.676	0.845	1.010
41	S-140-8-C50	3042	1.044	1.285	1.065	0.979	0.726	0.863	1.088
42	S-140-8-C50	3119	1.019	1.253	1.039	0.955	0.708	0.842	1.061
Mean value			1.090	1.198	1.046	0.943	0.692	0.841	1.004
Standard deviation			0.222	0.144	0.128	0.100	0.049	0.089	0.073
Coefficient of variation			0.204	0.120	0.122	0.106	0.071	0.106	0.073

(1) Stage OA ($0 < \varepsilon \leq \varepsilon_{scp}$):

$$\sigma = E_{sc}\,\varepsilon \tag{9}$$

where E_{sc} is the elastic modulus of the composite section and can be expressed as:

$$E_{sc} = f_{scp}/\varepsilon_{scp} \tag{10}$$

where f_{scp} and ε_{scp} are the stress and strain corresponding to point A in Fig. 16, and can be given as:

$$f_{scp} = [0.19 \cdot (f_{sy}/235) + 0.22 \cdot (30/f_c) + 0.13] \cdot \xi^{-0.2} \cdot f_{scy} \tag{11}$$

$$\varepsilon_{scp} = 3.01 \times 10^{-6} f_{sy} \tag{12}$$

where the unit for $f$sy and fc is N/mm^2

(2) Stage AB ($\varepsilon_{scp} < \varepsilon < \varepsilon_{scy}$):

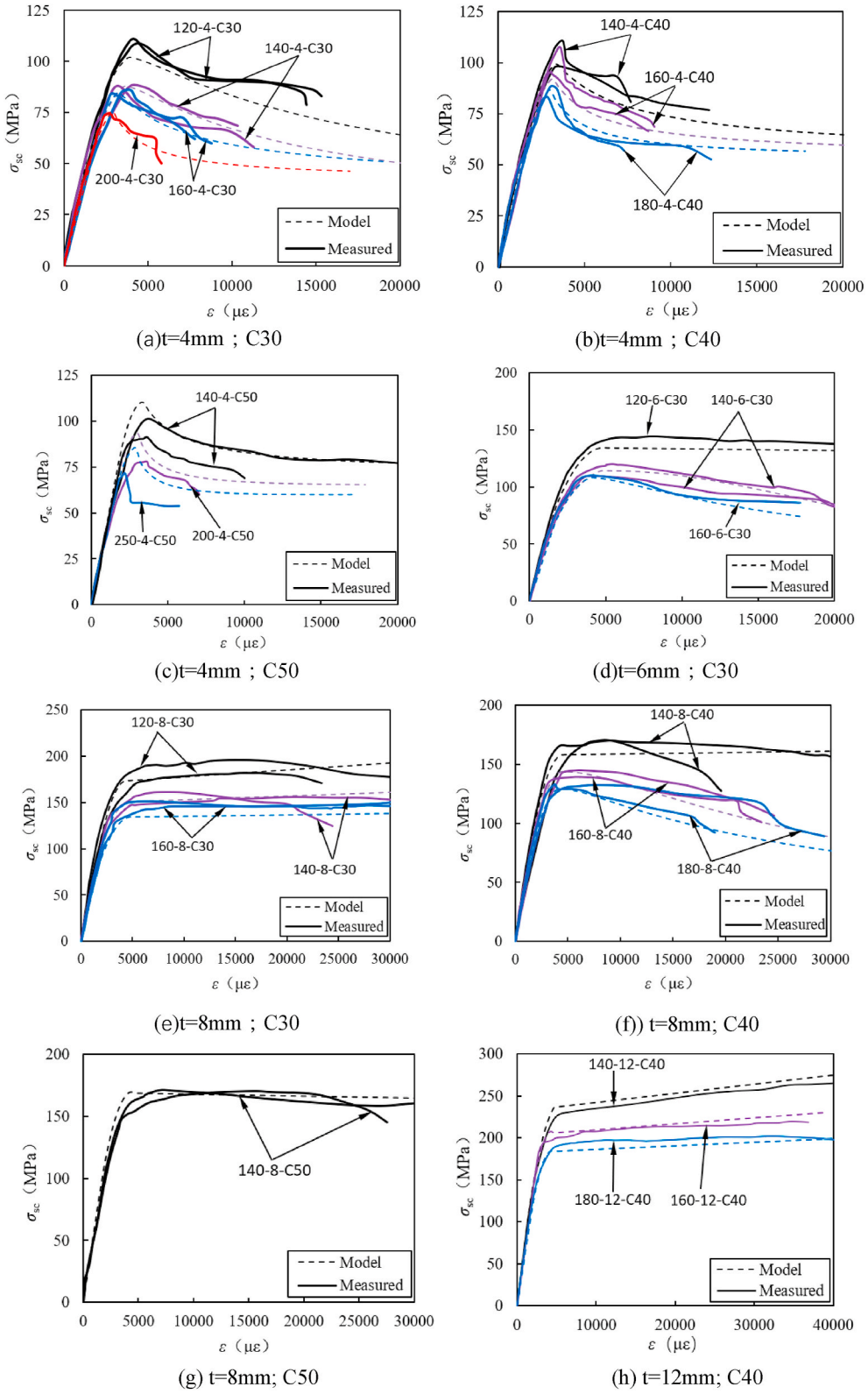

Fig. 18. Comparison of σ_{sc} versus ε curves between test results and mechanical model.

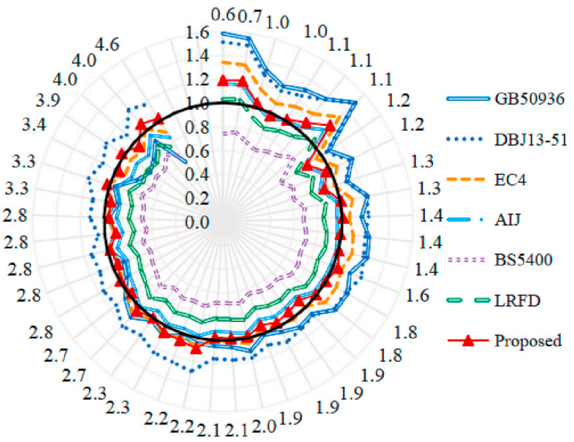

Fig. 19. Distribution of N_{uc}/N_{ue} with ξ.

In this stage, the mathematical relationship between σ_{sc} and ε can be given as Eqs. (13) and (14)

$$\sigma = f_{scp} + \left(f_{scy} - f_{scp}\right) \cdot \left\{ (1-\mathrm{k}) \cdot \left(\frac{\varepsilon - \varepsilon_{scp}}{\varepsilon_{scy} - \varepsilon_{scp}}\right)^2 + \mathrm{k} \cdot \left(\frac{\varepsilon - \varepsilon_{scp}}{\varepsilon_{scy} - \varepsilon_{scp}}\right) \right\} \tag{13}$$

$$k = 0.221 + 0.224\xi + 0.024 f_c \tag{14}$$

where the unit for f_c is N/mm^2.

(2) Stage BC ($\varepsilon \geq \varepsilon_{scy}$):

In this stage, σ_{sc} -ε can be expressed as

$$\sigma = \begin{cases} f_{scy} + E_{sch} \cdot \left(\varepsilon - \varepsilon_{scy}\right) & (\xi \geq 2.8 or \rho > 0.25) \\ f_{scy} \cdot \left\{ \left(\varepsilon / \varepsilon_{scy}\right) \cdot \left[\beta \left(\frac{\varepsilon - \varepsilon_{scy}}{\varepsilon_{scy}}\right)^{\eta} + \frac{\varepsilon}{\varepsilon_{scy}} \right] - 1 \right\} & (\xi < 2.8) \end{cases} \tag{15}$$

in which

$$E_{sch} = 520\xi - 1310 \tag{16}$$

$$\beta = 51.2 f_c^{-1} \cdot \exp\left(-0.43\xi^2\right) \tag{17}$$

$$\eta = -0.65 \ln \beta + 36.9 / f_c \tag{18}$$

where the unit for ε is 10^{-6}.

As a three-stage curve model, the geometric characteristics expressed by the model fully correspond to the compression deformation and failure process of SCCFDSSs, i.e

When $\sigma = 0$, $\varepsilon = 0$;

When $0 < \sigma < \sigma_B$, $d\sigma^2/d\varepsilon^2 = 0$, that is, the slope of the curve remains unchanged;

When $\sigma_B < \sigma < f_{scy}$, $d\sigma^2/d\varepsilon^2 < 0$, that is, the slope of the curve decreases monotonically without inflection point;

When $\sigma = f_{scy}$, $\varepsilon = \varepsilon_{scy}$, naming the nominal peak point;

When $\xi < 2.8$, the post peak curve shows a degradation trend, and when $\varepsilon \to \infty$, $\sigma \to 0$;

When $\xi \geq 2.8$, the post peak curve exhibits strain hardening behavior or elastic-perfectly plastic behavior, and the curve increases approximately linearly;

Fig. 18 compares the calculated σ_{sc}–ε relation curves between the tests and the mechanical model. It can be seen that good agreement is achieved.

5. Comparisons with current code provisions

For precisely assessing the section bearing capacities of the novel composite column proposed in this study, the design methods, including LRFD-1999 [31], AIJ-2008 [32], BS5400-2005 [33], EC4-2004 [25], GB 50936-2014 [34], DBJ13-51-2010 [35] are selected for comparison. To improve the comparability between each code, the safety factors of the material were unified.

The bearing capacity (N_{uc}) calculated using the different methods are compared with the 42 experimental results (N_{ue}) in Table 4,

respectively. Besides, the mean value of N_{uc}/N_{ue} and the corresponding standard deviation are also listed in Table 4. It can be seen from Table 4 that the bearing capacity given by LRFD-1999, AIJ-2008 and BS5400-2005 is about 6%–31% lower than the test results, while that by GB 50936-2014, DBJ13-51-2010 and EC4-2004 is averagely 5%–20% higher. The bearing capacity given by GB50936-2014 is significantly higher if ξ is less than 2.0, but evidently conservative if ξ exceed 2.0, which leads to large discreteness of N_{uc}/N_{ue} (with a COV of 0.204).

Generally, the above codes are incapable of predicting the structural performance of SCCFDSSTs. The omnidirectional prediction effect (N_{uc}/N_{ue}) is summarized in Fig. 19, which is a radar chart and visually shows the prediction effect of existing codes. Here, the radial coordinate represents N_{uc}/N_{ue}, ranging from 0 to 1.6. The circumferential coordinate represents ξ, ranging from 0.58 to 4.61. Each curve represents the overall distribution of N_{uc}/N_{ue} corresponding to the methods mentioned above.

It can be seen that among the six standards, the bearing capacity predicted by EC4-2004 method is the closest to the experimental results, with an average value of 1.046 and COV of 0.122. In contrast, the calculation formula proposed in this paper gives a mean of 1.004 and a COV of 0.073, which owns the best prediction effect.

6. Conclusions

This study describes a series of experiments on coral concrete-filled square DSST columns under axial compression. The influence of the constraint factor (ξ) and the ratio of width to wall thickness (B/t) on the performance of these coral concrete-filled DSST columns are analyzed in this study. A total of seven design methods (GB50936-2014, DBJ13-51-2010, EC4-2004, AIJ-2008, BS5400-2005, LRFD-1999, and the proposed method) are used to predict sectional strength, and the results are compared. The main conclusions of research findings can be drawn as follows:

(1) A novel square coral concrete-filled duplex stainless steel tube (SCCFDSST) is proposed, and the composite action provided by coral concrete and duplex stainless-steel tubes is sufficient.
(2) ξ, concrete strength, and B/t all represent the composite action of coral concrete and steel tube. In contrast, the influence of B/t on the mechanical behavior of SCCFDSSTs is very significant, while that of coral concrete strength is relatively moderate.
(3) SCCFDSSTs present satisfying ductility and bearing capacities, and the strength index (SI) and ductility index (DI) of SCCFDSSTs increase with the increase of ξ. It is suggested that the B/t should not exceed 50 in order to ensure the ductility of composite columns.
(4) A linear relationship is obtained between the sectional strength enhancement coefficient ($N_{ue}/A_{sc}f_c$) and ξ.
(5) A mechanical model is established for calculating the sectional capacity and the relationship between axial load and axial deformation of SCCFDSSTs, giving good agreement with test results.
(6) The design methods of current code are incapable of accurately predicting the bearing capacity of SCCFDSSTs, and the formulas proposed in this paper can provide more accurate prediction.

Author statement

Lan Rao: Writing; Formal analysis; Experiments.
Qingrui Yue: Funding acquisition; Conceptualization.
Bin Huang: Writing; Language polishing.
Xiao-gang Liu: Methodology; Project administration; Funding acquisition.

Declaration of competing interest

The authors declare that they have no known competing financial interests or personal relationships that could have appeared to influence the work reported in this paper.

Acknowledgment

The authors gratefully appreciate financial support provided by the National Natural Science Foundation of China (51890903), the Beijing Nova Program (Z201100006820044), the Henan Province Young Backbone Teacher Training Plan of China (2019GZGG075), and the National Key Research and Development Program of China (2017YFC0703403).

References

[1] Y.A. Yong, B. Dza, B. Sga, B. Zza, B. Csa, A review on the deterioration and approaches to enhance the durability of concrete in the marine environment, Cement Concr. Compos. 113 (2020), 103695.
[2] T.U. Mohammed, T. Yamaji, H. Hamada, Chloride diffusion, microstructure, and mineralogy of concrete after 15 years of exposure in tidal environment, ACI Mater. J. 99 (3) (2002) 256–263.
[3] G. Dempsey, Coral and salt water as concrete materials, ACI Mater. J. 23 (1951) 157–166.
[4] R. Ehlert, Coral concrete at Bikini atoll, Concr. Int. 13 (1) (1991) 19–24.
[5] P.A. Howdyshell, The Use of Coral as an Aggregate for Portland Cement Concrete Structures, Army Construction Engineering Research Laboratory, Champaign, 1974.
[6] A. Mrema, S. Bungara, Achieving high strength/high performance concrete from coral-limestone aggregates using ordinary Portland cement, fly ash and superplasticizer, in: 6th International Conference on Structural Engineering, Mechanics and Computation, 2016, pp. 1380–1385.
[7] H. Ootani, T. Ohoka, M. Tobisaka, Properties of Coral Aggregate and Coral Concrete in Miyakojima, Annual Meeting of the Architectural Institute of Japan, Tokyo, Japan, 1985.

[8] Q. Hu, T. Yang, Z.Z. Wang, Analysis of life cycle cost of frp marine coral concrete structure and common reinforced concrete structure, Construct. Econom. 37 (1) (2016) 61–66 ([in Chinese]).
[9] H.B. Yu, Z.X. Sun, C. Tang, Physical and mechanical properties of coral sand in the nansha islands, Mar. Sci. Bull. 8 (2) (2006) 31–39.
[10] J.M. Liu, Z.W. Qu, W. Peng, et al., Literature review of coral concrete, Arabian J. Sci. Eng. 43 (4) (2018) 1529–1541.
[11] B. Da, H.F. Yu, H.Y. Ma, et al., Chloride diffusion study of coral concrete in a marine environment, Construct. Build. Mater. 123 (2016) 47–58.
[12] B. Da, H. Yu, H. Ma, et al., Experimental investigation of whole stress-strain curves of coral concrete, Construct. Build. Mater. 122 (30) (2016) 81–89.
[13] X. Dou, H.F. Yu, H.Y. Ma, et al., Experiment on chloride diffusion coefficient of coral concrete exposed to marine environment, Ocean. Eng. 35 (1) (2017) 129–135 ([in Chinese]).
[14] P. Wattanachai, N. Otsuki, T. Satio, et al., A study on chloride ion diffusivity of porous aggregate concretes and improvement method, Dob. Gakkai Ronbunshu 65 (1) (2009) 30–44.
[15] S. Kakooei, H.M. Akil, A. Dolati, et al., The corrosion investigation of rebar embedded in the fibers reinforced concrete, Construct. Build. Mater. 35 (2012) 564–570.
[16] CECS410-2015, Technical Specification for Stainless Steel Structures, China Planning Press, Beijing, China, 2015 ([in Chinese]).
[17] J.A. Platt, A. Guzman, A. Zuccari, et al., Corrosion behavior of 2205 duplex stainless steel, Am. J. Orthod. Dentofacial Orthop. 112 (1) (1997) 69–79.
[18] L. Jin, L. Fan, P. Li, et al., Size effect of axial-loaded concrete-filled steel tube columns with different confinement coefficients, Eng. Struct. 198 (2019) 109503.
[19] L.H. Han, G.H. Yao, X.L. Zhao, Tests and calculations for hollow structural steel (HSS) stub columns filled with self-consolidating concrete (SCC), J. Constr. Steel Res. 61 (9) (2005) 1241–1269.
[20] GB/T 228.1-2010, Metallic Materials-tensile Testing-Part 1: Method of Test at Room Temperature, Standards Press of China, Beijing, China, 2010 ([in Chinese]).
[21] GB/T 50081-2019, Standard for Method of Mechanical Properties on Ordinary Concrete, China Architecture and Building Press, Beijing, China, 2019 ([in Chinese]).
[22] L. Li, Research on the Basic Properties of Coral Concrete, Doctoral thesis, Guangxi University, Nanning, China, 2012 ([in Chinese]).
[23] GB50017-2017, Standard for Design of Steel Structures, China Architecture and Building Press, Beijing, China, 2017 ([in Chinese]).
[24] W.Q. Liang, X.G. Wang, Z. He, Influence of GGBFS content on shrinkage cracking of concrete, Eng. J. Wuhan Univ. 37 (1) (2004) 77–81 ([in Chinese]).
[25] EN 1994-1-1:2004, Eurocode 4, Design of Composite Steel and Concrete Structures, Part 1-1: General Rules and Rules for Buildings, European Committee for Standardization, Brussels, Belgium, 2004.
[26] M. Su, Y. Cai, X. Chen, et al., Behavior of concrete-filled cold-formed high strength steel circular stub columns, Thin-Walled Struct. 157 (2020) 107078.
[27] L.H. Han, Tests on stub columns of concrete-filled RHS sections, J. Constr. Steel Res. 58 (3) (2002) 353–372.
[28] C. Petrus, H.A. Hamid, A. Ibrahim, et al., Experimental behaviour of concrete filled thin walled steel tubes with tab stiffeners, Steel Construct. 66 (7) (2010) 915–922.
[29] L.H. Han, Concrete-filled Steel Tubular Structures (The Third Version), China Science Press, Beijing, China, 2004 ([in Chinese]).
[30] B. Liu, J.H. Guo, J.K. Zhou, et al., The mechanical properties and microstructure of carbon fibers reinforced coral concrete, Construct. Build. Mater. 249 (2020) 118771.
[31] AISC-LRFD, Load and Resistance Factor Design Specification for Structural Steel Buildings, American Institute of Steel Construction, Chicago, USA, 1999.
[32] AIJ, Recommendations for Design and Construction of Concrete Filled Steel Tubular Structures, Architectural Institute of Japan, Tokyo, Japan, 2008.
[33] BS5400, Steel, Concrete and Composite Bridges, Part 5: Code of Practice for Design of Composite Bridges, British Standards Institution, London, UK, 2005.
[34] GB 50936-2014, Technical Code for Concrete Filled Steel Tubular Structures, China Architecture and Building Press, Beijing, China, 2014 ([in Chinese]).
[35] DBJ/T13-51-2010, Technical Specification for Concrete-Filled Steel Tubular Structures, The Construction Department of Fujian Province, Fuzhou, China, 2010 ([in Chinese]).